

# Structurally Tolerance-Factor-Tuned Metal Halide Nanocrystals for Environmentally Stable and Efficient Red Light-Emitting Diodes

Xuehai Fu, Wen Li,\* Xiankan Zeng, Cheng Yan, Xiaodong Peng, Yue Gao, Qungui Wang, Jingjing Cao, Shiyu Yang, and Weiqing Yang\*



Cite This: *J. Phys. Chem. Lett.* 2022, 13, 2217–2225



Read Online

ACCESS |



Metrics & More

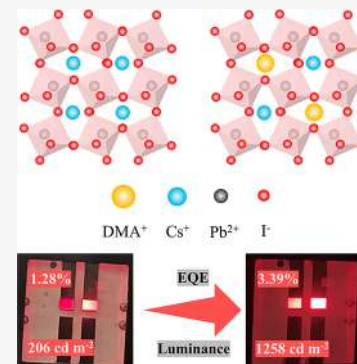


Article Recommendations



Supporting Information

**ABSTRACT:** Black phase CsPbI<sub>3</sub>, naturally possessing the superiority of high radiative recombination efficiency and narrow emission line width, shows promise for commercial applications of red perovskite light-emitting diodes (PeLEDs). However, the metastable black phase CsPbI<sub>3</sub> with a marginal tolerance factor ( $t$ ) of 0.81 would easily convert to the nonoptical yellow phase. Herein, we demonstrate the strategy of partial substitution of larger dimethylammonium cation (DMA<sup>+</sup>) for Cs<sup>+</sup> to achieve the stable tolerance factor of 0.903 for greatly improved Cs<sub>0.7</sub>DMA<sub>0.3</sub>PbI<sub>3</sub> nanocrystals. These NCs present a superior ultraviolet (UV) irradiation stability by retaining 80% of the initial photoluminescence intensity after 5 h, which is much better than that of its counterparts (retaining 30%). Based on this, the as-developed red PeLEDs demonstrate remarkable luminance of 1258 cd/m<sup>2</sup> and external quantum efficiency of 3.39%, which are almost 6 times and 3 times that of its counterparts, respectively (206 cd/m<sup>2</sup> and 1.28%). This strategy may pave the way to improving the stability and efficiency of PeLEDs.



Metal halide perovskites (MHPs), a newly emerged excellent and potential semiconductor material, yield unusually brilliant results in the field of perovskite light-emitting diodes (PeLEDs).<sup>1</sup> In particular, their unique high photoluminescence (PL) efficiency, narrow emission line width, and tunable emitting wavelength make them one of the most promising candidates for next-generation displays and illumination devices.<sup>2–8</sup> With sustained efforts in recent years, the stability of blue- and green-emitting perovskite NCs has shown significant improvement.<sup>9–11</sup> However, the black phase of MHPs (CsPbI<sub>3</sub>) with the edge tolerance factor ( $t$ ) of 0.81 will spontaneously and easily transform into a nonperovskite orthorhombic ( $\delta$ ) yellow phase at room temperature.<sup>12–17</sup> Such an undesired phase degradation process has greatly impeded the promotion of red light-emitting diode efficiency.<sup>18,19</sup> This exceedingly unbalanced development of the three primary colors triggered by the poor stability of red perovskite seriously hinders the further practical commercial application of PeLEDs.<sup>14,20,21</sup> Therefore, achieving high stability is still a huge challenge for commercial applications of red PeLEDs.

In this regard, there are two main strategies to stabilize the CsPbI<sub>3</sub> NCs structure for a long time: ligand engineering and component engineering.<sup>18,19,21–30</sup> For ligand engineering, the different length ligands on the surface of perovskite are usually employed to passivate the surface defects. Although many splendid contributions toward ligand engineering have greatly promoted the development of high-stability CsPbI<sub>3</sub> NCs, the addition of organic ligands will unavoidably decrease the conductivity of CsPbI<sub>3</sub> NCs and then limit its efficiency. For

component engineering, introducing differently sized ion A, B, and X sites of perovskite ABX<sub>3</sub> into CsPbI<sub>3</sub> NCs is usually employed to tune the tolerance factor to a more stable value toward high phase stability. According to the formula of tolerance factor  $t = \frac{(R_A + R_X)}{\sqrt{2}(R_B + R_X)}$ , it has been usually believed that a suitable range for perovskite is 0.8–1.10, whereas the calculated value of CsPbI<sub>3</sub> NCs is  $t = 0.81$ , which means it is difficult to maintain its structure at room temperature for a long time.<sup>16,17,31</sup> Presently, most component engineering strategies are implemented by introducing the smaller B-site cation to tune the tolerance factor for high stability, such as Cu<sup>2+</sup>, Zn<sup>2+</sup>, Ni<sup>2+</sup>, Sr<sup>2+</sup>, and Mn<sup>2+</sup>. However, Cs<sup>+</sup> as A-cation already is the maximum inorganic nonradioactive elemental cation. Thus, the larger organic cation has to be selected to tune the tolerance factor by A-site cation exchange. Among the organic cations, formamidinium (FA<sup>+</sup>) and methylammonium (MA<sup>+</sup>) occupying the A-site are often used to improve CsPbI<sub>3</sub> stability and device performance.<sup>1,32–35</sup> In addition, the larger organic cation not only tunes the parameters of the crystal structure of perovskite but also releases residual tensile strain and induces compressive strain in the lattice to increase the

Received: February 6, 2022

Accepted: February 25, 2022

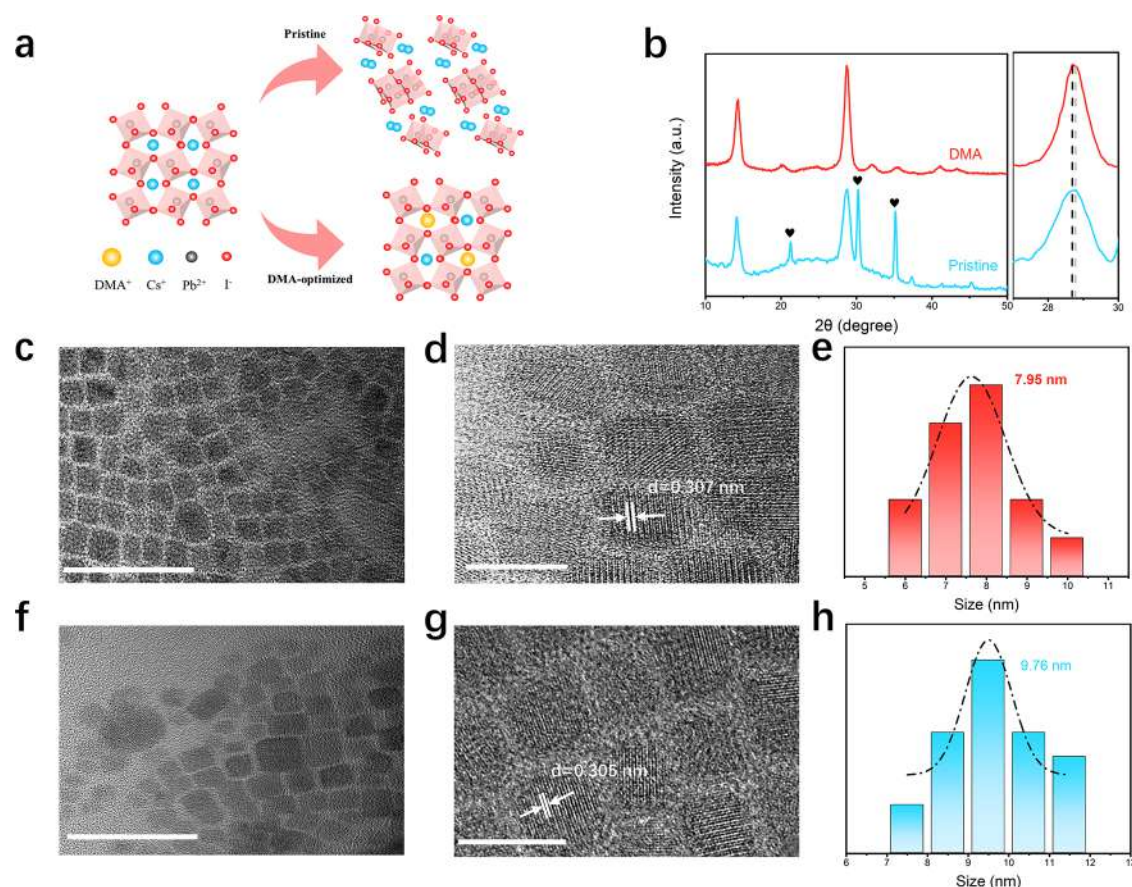


**Figure 1.** Characterization of pristine NCs and DMA-NCs. (a) Schematic image of the stabilization of phase structure with DMA<sup>+</sup>. (b) XRD patterns and enlarged partial peak. (c–f) TEM and HRTEM images and statistical chart of particle size distribution of DMA-NCs and pristine NCs. Scale bars are 50 nm in panels c and f and 10 nm in panels d and g.

energy of defect formation and stabilize CsPbI<sub>3</sub> NCs.<sup>36–38</sup> Therefore, introducing a larger A-site cation to theoretically tune the tolerance factor and enhance CsPbI<sub>3</sub> NC stability provides another efficient solution to resolve this issue.

In this work, we report the partial substitution strategy of larger dimethylammonium cation (DMA<sup>+</sup>) for Cs<sup>+</sup> to achieve the Cs<sub>0.7</sub>DMA<sub>0.3</sub>PbI<sub>3</sub> nanocrystals (DMA-NCs) with enhanced environmental stability, using DMA<sup>+</sup>-modified PbI<sub>2</sub> (DMA-PbI<sub>2</sub>). Such a substitution strategy can optimize structural tolerance factor and then release the tensile strain in NCs to increase the defect formation energy for the purpose of environmental stability. Benefiting from the release of residual strain in the CsPbI<sub>3</sub> lattice, these NCs present an excellent PLQY of 97.04% with a narrow full width at half-maximum (fwhm) of 33.4 nm, presenting a superior color purity among red perovskite NCs. Further, the partial substitution of DMA<sup>+</sup> for Cs<sup>+</sup> results in the remarkably increased exciton binding energy and longitudinal-optical (LO) photon energy, revealing that nonradiative recombination is effectively suppressed. Benefiting from these improvements, we developed the red PeLEDs with the remarkable luminance of 1258 cd/m<sup>2</sup> and external quantum efficiency of 3.39%. Therefore, we believe that this strategy may pave the way to achieve the practical commercial application of PeLEDs.

As shown in Figures 1c–h, the transmission electron microscopy (TEM) images clearly demonstrate the more regular and uniform shape of DMA-NCs in comparison to that of the pristine sample. Compared with a pristine sample (9.76

nm), the average sizes of DMA-NCs has decreased to 7.35 nm. In addition, the high-resolution TEM (HRTEM) images show that the pristine NCs and DMA-NCs are highly crystalline (Figures 1d,g). The interplanar distance of 0.305 nm corresponds to the (220) crystal plane of  $\gamma$ -CsPbI<sub>3</sub>.<sup>39</sup> Meanwhile, expanded-interplanar distance from 0.305 to 0.307 nm demonstrates successful substitution of DMA<sup>+</sup> for Cs<sup>+</sup>.<sup>37</sup> In Figure S3, the “black dots” of DMA-NCs almost disappear, evidently revealing the partial substitution of the larger DMA<sup>+</sup> for Cs<sup>+</sup> could effectively suppress these “black dots”. The black dots are Pb<sup>0</sup>, which is the result of electron beam-induced degradation of Pb<sup>2+</sup> to Pb<sup>0</sup>. Besides, the black dots have been proved to be nonradiative recombination centers, which would be detrimental to the optical properties and stability of NCs.<sup>40–42</sup> As shown in Figure 1b, the x-ray diffraction (XRD) was used to analyze crystalline structure and both samples possess the same crystalline structure as the  $\gamma$ -CsPbI<sub>3</sub>, which demonstrates that larger DMA<sup>+</sup> would not change the structure of NCs. Both samples exhibit strong peaks at 14.2° and 28.6°, which correspond to the (110) and (220) crystal planes in the  $\gamma$ -phase. In addition, the enlarged partial XRD patterns of 28–30° correspond to (220) peak of  $\gamma$ -CsPbI<sub>3</sub>. Compared with the pristine NCs, the peak of DMA-NCs shifts from 28.78° to a smaller angle of 28.68°, revealing that the successful substitution of the larger DMA<sup>+</sup> for Cs<sup>+</sup> indeed promotes the lattice expansion of DMA-NCs. It also confirms that the intrinsic residual strain could be released once the larger DMA<sup>+</sup> gets into the perovskite lattice, which

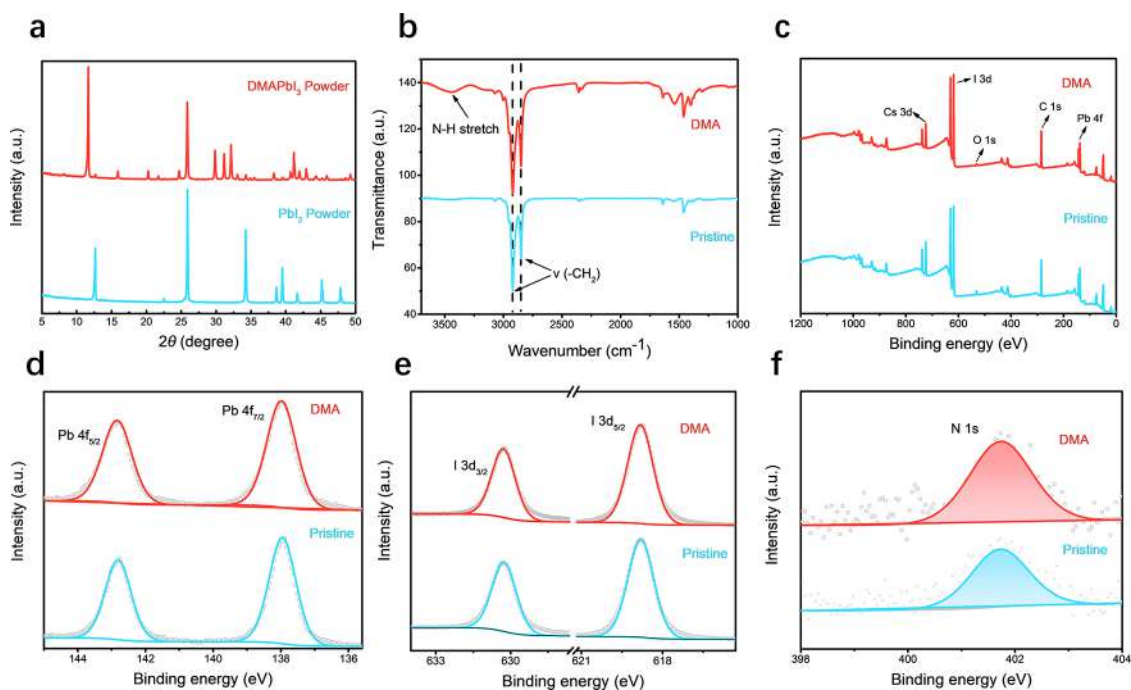


**Figure 2.** Characterization of DMAPbI<sub>3</sub> and PbI<sub>2</sub> powders and corresponding CsPbI<sub>3</sub> NCs. (a) XRD of DMAPbI<sub>3</sub> and PbI<sub>2</sub> powders. (b) FTIR of pristine NCs and DMA-NCs. (c) Total XPS spectra. XPS spectra of (d) Pb 4f, (e) I 3d, and (f) N 1s of pristine NCs and DMA-NCs.

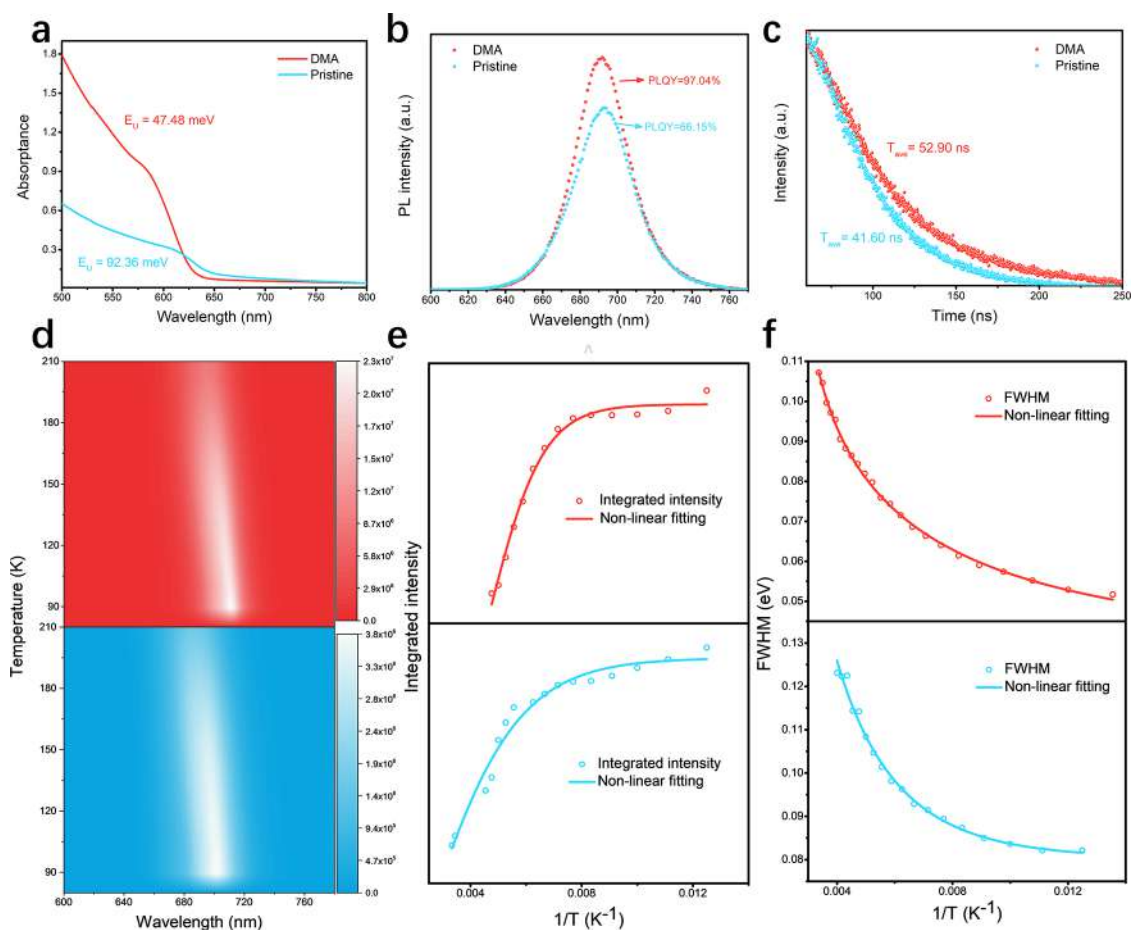


**Figure 3.** Optical properties and carrier dynamics analysis of DMA-NCs and pristine NCs. (a) UV-vis absorption spectra. (b) PL spectra and PLQY. (c) Time-resolved PL decay. (d) Temperature-dependent PL spectra of DMA-NCs (upper) and pristine NCs (lower). (e) Integrated PL intensity as a function of temperature of DMA-NCs (upper) and pristine NCs (lower). (f) fwhm as a function of temperature of DMA-NCs (upper) and pristine NCs (lower).



would increase the energy of defect formation and then enhance the relative activation energies for the vacancy-assisted migration of halide ions.<sup>36</sup> The DMA-NCs can be stored for several months, indicating its excellent environmental stability (Figure S6). Further, Figure 1a sketches the phase transition process of both samples. For the optimal sample, the partial substitution of the larger DMA<sup>+</sup> for Cs<sup>+</sup> can effectively prevent it from transitioning to the yellow phase, substantially improving the stability of NCs. Whereas for pristine NCs, the phase transition from black phase to nonoptical yellow phase will happen in a short time.

Owing to the substitution of DMA<sup>+</sup> for Cs<sup>+</sup>, excellent environmental stability can be achieved. In this work, the DMAPbI<sub>3</sub> is used to synthesize the Pb precursor instead of traditional method by PbI<sub>2</sub>, which favors substituting DMA<sup>+</sup> for Cs<sup>+</sup>. Fourier transform infrared spectrometer (FTIR) characterization was used to analyze the as-synthesized DMAPbI<sub>3</sub> powder. In Figure S4, the FTIR spectrum confirms the presence of N–H and C–H bonds. The distinct characteristic peaks including N–H stretching mode (3200–3450 cm<sup>-1</sup>), N–H bending mode (1200–2000 cm<sup>-1</sup>), and C–H bending mode (1490–1350 cm<sup>-1</sup>) are associated with DMA<sup>+</sup>, indicating that the larger DMA<sup>+</sup> was successfully introduced into the PbI<sub>2</sub> powder.<sup>43</sup> Also, XRD was used to further confirm whether DMAPbI<sub>3</sub> is synthesized successfully or not. As shown in Figure 2a, the XRD pattern of the synthesized DMAPbI<sub>3</sub> powder presents peaks at 11.6°, 25.8°, 31.1°, 32.1°, 41.1°, and 42.8°, which can be consistent with DMAPbI<sub>3</sub>.<sup>12,43</sup> In addition, the scanning electron microscopy (SEM) image can evidently affirm the formation of DMAPbI<sub>3</sub> rods, and energy-dispersive spectrometric (EDS) mapping can clearly ensure the uniform distribution of element N in the “rods”.<sup>43,44</sup> All these results strongly indicate the successful synthesis of DMAPbI<sub>3</sub> powder (Figure S1).

Furthermore, FTIR was also used to analyze pristine NCs and DMA-NCs; a N–H stretch mode (3200–3450 cm<sup>-1</sup>) appears in DMA-NCs, which corresponds to the N–H stretch mode of DMAPbI<sub>3</sub> powder in Figure S4.<sup>43</sup> This indicates the larger DMA<sup>+</sup> has been successfully substituted for Cs<sup>+</sup> in CsPbI<sub>3</sub> NCs (Figure 2b). To ascertain the interaction between DMA<sup>+</sup> and CsPbI<sub>3</sub> NCs, X-ray photoelectron spectroscopy (XPS) characterization was conducted to analyze the chemical states of elements in the perovskite. These XPS results evidently revealed both samples should contain the elements of Cs, Pb, I, C, and N (Figure 2c). Compared with pristine NCs, the high-resolution XPS spectra show that the binding energy of Pb 4f<sub>5/2</sub> and 4f<sub>7/2</sub> for DMA-NCs shifts from 137.88 and 142.74 eV to higher binding energy of 137.95 and 142.80 eV (Figure 2d), while I 3d<sub>3/2</sub> and 3d<sub>5/2</sub> binding energy peaks shift from 618.70 and 630.16 eV to higher binding energies 618.82 and 630.28 eV, respectively (Figure 2e). The increased binding energy between DMA and Pb/I is ascribed to the successful substitution of the larger DMA<sup>+</sup> for Cs<sup>+</sup>. In addition, N signal peaks appear in both samples; the peak area of DMA-NCs increases about 35% in Figure 2f. Compared with the pristine NCs, the Cs/Pb atomic ratio of DMA-NCs decreases from 1.20 to 0.98, while the atomic ratio of N/Pb increases from 0.89 to 1.26. Evidently, these results reconfirm that the larger DMA<sup>+</sup> should partially substitute Cs<sup>+</sup> in CsPbI<sub>3</sub> NCs.<sup>19,21,25</sup>

The UV–vis absorption and PL spectra were obtained to investigate the optical properties of pristine NCs and DMA-NCs, and the results are shown in Figures 3a,b. The Urbach energy ( $E_U$ ) was calculated from the absorption coefficient and

function of the photon energy of the UV-absorption spectra. In the semiconductor, the absorption edge is regarded as the Urbach tail, which is generally related to the degree of crystal disorder.<sup>45</sup> And the calculating formular is as follows:

$$\alpha = \alpha_0 e^{(h\nu/E_U)} \quad (1)$$

$$\ln \alpha = \ln \alpha_0 + (h\nu/E_U) \quad (2)$$

where  $\alpha$  is the absorption coefficient as a function of photon energy,  $\alpha_0$  a characteristic parameter of the material, and  $h$  Planck's constant. The  $E_U$  value of DMA-NCs is calculated to be 47.48 meV, which is lower than that of pristine CsPbI<sub>3</sub> NCs (92.36 meV). This lower  $E_U$  value directly demonstrates a lower density of defects and the more ordered crystal structure after the partial substitution. In addition, the PLQY of DMA-NCs and pristine NCs were determined by using a fluorescence spectrometer equipped with an integrating sphere with excitation wavelength at 365 nm, and PLQYs of both samples in toluene solution are shown in Figure 3b. The PLQY of DMA-NCs increases from 66.15% to 97.04%, a nearly 50% improvement. Such a substantial enhancement of PLQY demonstrates that plenty of defects should be effectively passivated and nonradiative combination can be strongly suppressed by DMA<sup>+</sup>. Meanwhile, the stronger intensity of the PL spectrum and narrower fwhm of 33.4 nm for DMA-NCs in comparison to that of pristine NCs of 36.9 nm obviously demonstrate the better crystallinity and high color purity. In Figure 3c, time-resolved photon luminance (TRPL) decay measurement spectra indicate the calculated average PL lifetime of DMA-NCs rises to 52.90 ns from 41.60 ns. Furthermore, the time-resolved PL curves can be fitted by biexponential decay functions, including the fast decay component ( $\tau_1$ ) which connects with the nonradiative recombination of initially photogenerated carriers and the slow decay ( $\tau_2$ ) which connects to the bimolecularly radiative recombination of charge carrier.<sup>11</sup> The fitted parameters are summarized in Table S1. The calculated nonradiative decay rate of DMA-NCs is  $5.595 \times 10^5 \text{ s}^{-1}$ , which is an order of magnitude lower than that of pristine NCs ( $8.137 \times 10^6 \text{ s}^{-1}$ ), and the radiative decay rate of DMA-NCs increases from  $1.5901 \times 10^7 \text{ s}^{-1}$  to  $1.8344 \times 10^7 \text{ s}^{-1}$  simultaneously. Therefore, all the results indicate that DMA<sup>+</sup> can indeed reduce the density of trap states, which is mainly ascribed to the higher defect formation energy caused by release of residual strain.<sup>46</sup> Fewer defects will usually increase radiative combination and reduce nonradiative combination in perovskites, which favors the better performance of PeLEDs.

Furthermore, temperature-dependent PL spectroscopy was used to study the photophysical properties and carrier dynamics. Both pristine NCs and DMA-NCs show strong dependence of PL intensity and full width at half-maximum (fwhm) on temperature (Figure 3d). As shown in Figures 3d and S5, the PL peak intensity reduces and the fwhm broadens as temperature increases. This reduced PL peak intensity should originate from defect-induced quenching. In addition, their PL peak wavelength shift indicates the bandgap energy increases as temperature increases. Such a shift may originate from band renormalization by exciton–longitudinal optical (LO) photon. In addition, their strong dependence of fwhm on temperature implies strong exciton–photon interaction, which is dominated by exciton–LO phonons.

The Arrhenius equation was used to calculate the exciton binding energy ( $E_b$ ) of both samples, as follows:

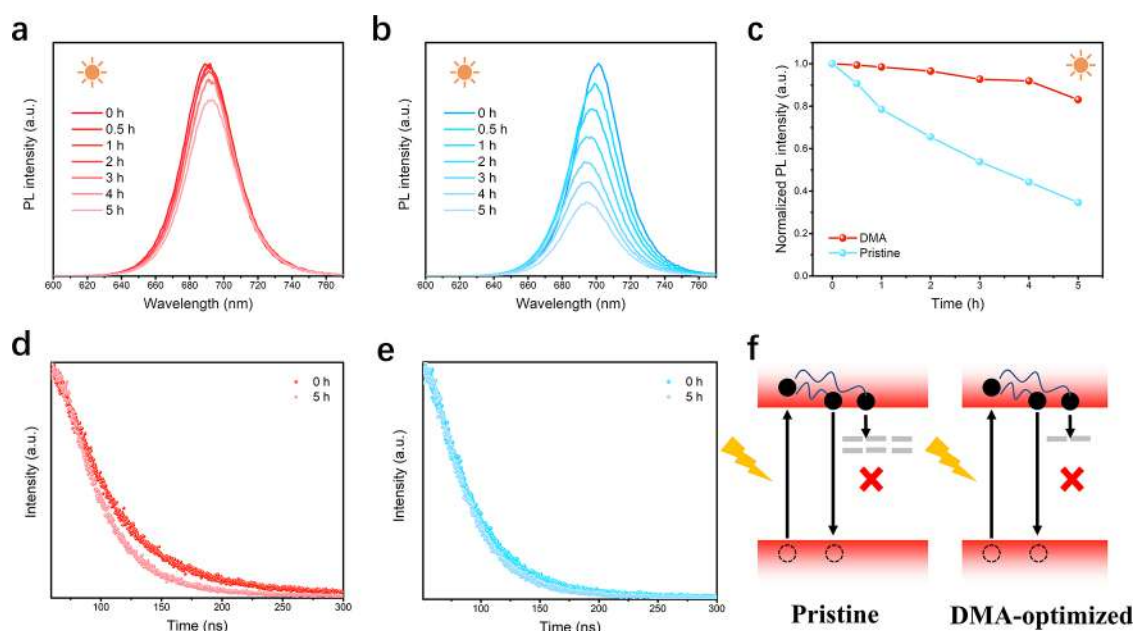


**Figure 4.** Stability analysis. PL spectra of the DMA-NCs (a) and pristine NCs (b) films under continuous UV light radiation (365 nm, 36 W). (c) Normalized PL intensity of pristine and DMA-NCs films under different UV light radiation time intervals. Time-resolved PL decay before and after UV light radiation of the DMA-NC (d) and pristine NC (e) films. (f) Schematics of radiative and nonradiative recombination of pristine NCs and DMA-NCs.

$$I(T) = I_0 / (1 + Ae^{-E_b / (k_B T)}) \quad (3)$$

where  $I_0$  is the PL intensity of 80 k,  $E_b$  the exciton binding energy,  $A$  the pre-exponential coefficient, and  $k_B$  the Boltzmann constant. In Figure 3e, compared with the pristine NCs, the  $E_b$  of DMA-NCs increases from 51.36 to 88.78 meV, evidently revealing the greatly improved suppression effect on nonradiative combination and then the greater exciton recombination behavior. Such obvious improvement makes it an excellent candidate for PeLEDs.

The boson model was used to indicate the relationship between temperature and fwhm, as follows:

$$\Gamma(T) = \Gamma_{\text{inh}} + \sigma T + \frac{\Gamma_{\text{LO}}}{e^{E_{\text{LO}} / (k_B T)} - 1} \quad (4)$$

where  $\Gamma_{\text{inh}}$  is the inhomogeneous broadening coefficient, which is connected with the size, shape, and composition of the perovskite nanocrystals and is temperature-independent;  $\sigma$  is the exciton–acoustic photon coupling coefficient, relating to the linear temperature-dependent deformation potential interaction;  $\Gamma_{\text{LO}}$  represents the exciton–LO photon coupling coefficient; and  $E_{\text{LO}}$  is the LO photon energy. The acoustic photons dominate the exciton–photon interaction as the LO phonon population is significantly reduced in the low-temperature regime ( $T < 100$  K), and high-energy LO photons dominate the exciton–photon interaction as the temperature increases to the high-temperature region. The as-measured fwhm data was fitted through eq 4, which is presented in Table S2. In Figure 3f, for pristine NCs,  $\Gamma_{\text{inh}} = 80.44$  meV,  $\Gamma_{\text{LO}} = 190$  meV, and  $E_{\text{LO}} = 35.07$  meV; while for DMA-NCs,  $\Gamma_{\text{inh}} = 31.17$  meV,  $\Gamma_{\text{LO}} = 437$  meV, and  $E_{\text{LO}} = 173.63$  meV. In the same temperature regime, the narrower fwhm variation of DMA-NCs indicates the less effect of lattice vibrations on excitons than pristine NCs. Both LO photon energy  $E_{\text{LO}}$  and exciton–longitudinal (LO) photon coupling coefficient  $\Gamma_{\text{LO}}$  of DMA-NCs remarkably increased, indicating

good suppression effect of nonradiative combination and strong exciton–photon interaction.<sup>47,48</sup> Overall, along with the environmental stability improvement of DMA-NCs, the increased exciton binding energy and LO photon energy evidently reconfirm that the larger DMA<sup>+</sup> can substantially suppress exciton dissociation and dramatically increase the population of excitation-generated electron–hole pairs in luminescing states, effectively suppressing the nonradiative combination of PeLEDs. Therefore, for PeLEDs, the less electron–hole pair quenching there is, the better the PeLED performance.

A portable UV lamp with a wavelength of 365 nm and an intensity of 36 W was employed to measure the environmental stability of pristine NCs and DMA-NCs. As shown in Figure 4a,b, the decreased PL intensity of DMA-NCs is much slower than that of pristine NCs after 5 h of UV exposure ( $7 \times 10^{-2}$  W cm<sup>-2</sup>). In Figure 4c, the PL intensity of DMA-NCs remains at about 80% of the initial PL intensity, much better than that of pristine NCs (retaining 30%) after 5 h of UV exposure, indicating the larger DMA<sup>+</sup> could improve the environmental stability of NCs. In Figure 4d,e, although both of them decay after 5 h of UV exposure, the fitted lifetime of DMA-NCs (41.50 ns) is still longer than that of pristine NCs (38.24 ns), demonstrating less defect-caused nonradiative combination of DMA-NCs in comparison to pristine NCs. The behavior of the electron and hole shift is sketched in Figure 4f. Compared with pristine NCs, DMA-NCs present fewer defects, which is ascribed to the high energy of defect formation caused by larger DMA<sup>+</sup>. Such reduction effect on defects results in the effective suppression of nonradiative combination, achieving excellent emission properties. In addition, the substitution of DMA<sup>+</sup> for Cs<sup>+</sup> would release partial residual strain and induce compressive strain, which will increase the activation energy for ion migration and then achieve excellent environmental stability. In addition, the pristine NC films show peaks at 26.46° and 37.64° only after 4 days, which correspond to

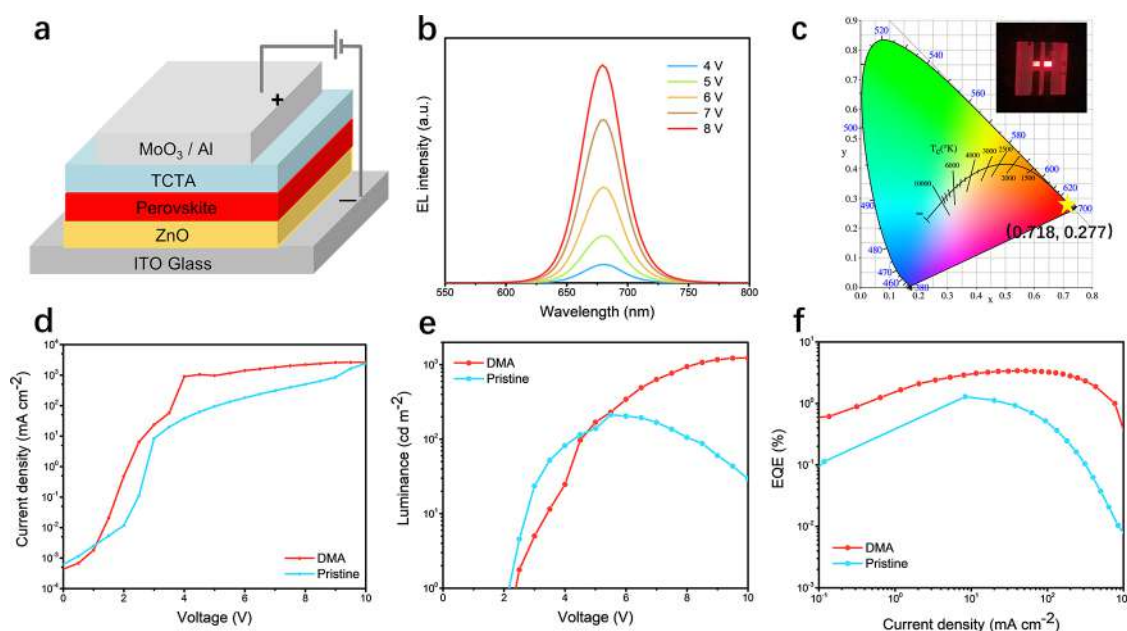


**Figure 5.** Red PeLED device fabrication and performance. (a) Device structure of as-fabrication PeLEDs. (b) Normalized EL spectra of PeLEDs based on DMA-NCs. (c) Commission Internationale de l’Eclairage (CIE) color coordinates of DMA-NC-based LED. Inset: A photograph of DMA-NCs-based PeLED at 8.0 V. (d) Current density–voltage curves. (e) Luminance–voltage curves. (f) EQE–current density curves.

(105) and (020) crystal planes of the  $\delta$ -phase. In addition, the peaks of  $14.20^\circ$  and  $28.6^\circ$  disappear, which correspond to the (110) and (220) crystal planes of  $\gamma$ -phase.<sup>49</sup> The DMA-NCs films present unchangeable peaks of  $\gamma$ -phase under the same conditions (Figure S4). Evidently, the partial substitution of the larger DMA<sup>+</sup> for Cs<sup>+</sup> can indeed reduce trap states for the greatly improved environmental stability of red CsPbI<sub>3</sub> NCs, which is a long sought-after result for easy phase transition.

On the basis of DMA-NCs, we developed the PeLED device to demonstrate how the DMA<sup>+</sup> caused high phase stability and superior charge transport to improve PeLED performance. Figure 5a schematically illustrates the PeLED device architecture of ITO/ZnO/NCs/TCTA/MoO<sub>3</sub>/Al. In Figure 5b, this PeLED exhibits pure red stable electroluminescence (EL) spectra of 680 nm with fwhm of 41 nm, corresponding to the Commission Internationale de l’Eclairage (CIE) color coordinates of (0.718, 0.277) (Figure 5c). Its current density rises faster than that of pristine NCs (Figure 5d), which indicates the larger DMA<sup>+</sup> can effectively reduce the trap states and be beneficial for the efficient charge injection in the emitting layer. As shown in Figure 5d, their voltage–luminance curves both show the lower turn-on voltage of about 2 V in comparison to those of other works (Table S3). Furthermore, the PeLEDs for DMA-NCs show maximum luminance of 1258 cd m<sup>-2</sup>, which is more than 6 times that of pristine NCs (203 cd m<sup>-2</sup>) (Figure 5e). In addition, its maximum external quantum efficiency (EQE) is 3.39%, which is almost 3 times that of pristine NCs (1.28%) (Figure 5f). Such greatly improved performance of PeLEDs based on DMA-NCs can be ascribed to the high quality of NCs films and more effective radiative recombination behavior.<sup>23,33,50</sup> For PeLEDs based on pristine NCs, carriers would be captured by plenty of defects, which would cause nonradiative combination, resulting in poor PeLED performance. All these results evidently reconfirm that the partial substitution of the larger DMA<sup>+</sup> for Cs<sup>+</sup> can greatly reduce the density of defects and effectively suppress nonradiative recombination behaviors, which results in

superior luminance and higher external quantum efficiency. In addition, PeLEDs based on pristine NCs would degrade faster than DMA-NCs under high voltage. As shown in Table S3, the as-developed PeLED performance is better and comparable with previously reported results achieved through hot injection methods.

The significant improvement of PeLED performance based on DMA-NCs is ascribed to superior tolerance factor induced high phase stability and release of tensile strain by the larger DMA<sup>+</sup> in the lattice. First, the metastable CsPbI<sub>3</sub> with marginal tolerance factor of 0.81 would easily and spontaneously undergo phase transition from black phase ( $\alpha$ ,  $\beta$ , and  $\gamma$ ) to yellow  $\delta$ -phase. Such a phase transition process could be expedited by the conditions of heat, light, and moisture. Therefore, the larger DMA<sup>+</sup> can tune the tolerance factor to improve the environmental stability of CsPbI<sub>3</sub>, which can be stored in ambient conditions for several months. Second, the larger DMA<sup>+</sup> expands the CsPbI<sub>3</sub> lattice, which would partially release the tensile strain and slightly induce compressive strain in the lattice. The residual strain in the perovskite lattice could significantly influence the energy of defect formation. In general, the energy of defect formation under tensile strain will be lower than that under compressive strain. Thus, fewer defects would form under such conditions of strain, resulting in more effective radiative recombination behavior of electrons and holes. Based on this, the as-fabricated PeLEDs exhibit superior performance in terms of luminance and external quantum efficiency. This substitution strategy of larger DMA<sup>+</sup> for Cs<sup>+</sup> not only results in superior tolerance factor but also optimizes the condition of strain in the lattice.

In summary, we have successfully demonstrated the partial substitution strategy of larger dimethylammonium cation (DMA<sup>+</sup>) for Cs<sup>+</sup> to achieve the stable tolerance factor of 0.903 for greatly improved CsPbI<sub>3</sub> nanocrystals (NCs). The larger DMA<sup>+</sup> regulates the size of NCs and releases residual strain in the lattice, which will improve the environmental stability of DMA-NCs. Moreover, the larger DMA<sup>+</sup> can reduce



the defects and increase the exciton binding energy and LO photon energy. As a result, the DMA-NCs show a higher PLQY of 97.04% in comparison to that of pristine NCs (66.15%). Based on DMA-NCs, the as-fabricated PeLEDs show maximum luminance of 1258 cd m<sup>-2</sup> and EQE of 3.39%, which are better than those of pristine NCs (203 cd m<sup>-2</sup> and 1.28%). Therefore, we believe that a structural tolerance-factor-tuned strategy will boost the development of environmental stability for NC and PeLED performance, which could lead to promising applications in optoelectronic devices.

## ■ ASSOCIATED CONTENT

### SI Supporting Information

The Supporting Information is available free of charge at <https://pubs.acs.org/doi/10.1021/acs.jpcllett.2c00361>.

SEM images, EDS images and FTIR images of DMAPbI<sub>3</sub>, TEM images of Pristine NCs, Temperature-dependent PL spectroscopy of Pristine NCs and DMA-NCs and photographs of aged DMA-NCs and pristine NCs (PDF)

## ■ AUTHOR INFORMATION

### Corresponding Authors

**Wen Li** – Key Laboratory of Advanced Technologies of Materials (Ministry of Education), School of Materials Science and Engineering, State Key Laboratory of Traction Power, Southwest Jiaotong University, Chengdu 610031, PR China; Email: [liwen3337@swjtu.edu.cn](mailto:liwen3337@swjtu.edu.cn)

**Weiqing Yang** – Key Laboratory of Advanced Technologies of Materials (Ministry of Education), School of Materials Science and Engineering, State Key Laboratory of Traction Power, Southwest Jiaotong University, Chengdu 610031, PR China; [orcid.org/0000-0001-8828-9862](https://orcid.org/0000-0001-8828-9862); Email: [wqyang@swjtu.edu.cn](mailto:wqyang@swjtu.edu.cn)

### Authors

**Xuehai Fu** – Key Laboratory of Advanced Technologies of Materials (Ministry of Education), School of Materials Science and Engineering, State Key Laboratory of Traction Power, Southwest Jiaotong University, Chengdu 610031, PR China

**Xiankan Zeng** – Key Laboratory of Advanced Technologies of Materials (Ministry of Education), School of Materials Science and Engineering, State Key Laboratory of Traction Power, Southwest Jiaotong University, Chengdu 610031, PR China

**Cheng Yan** – Key Laboratory of Advanced Technologies of Materials (Ministry of Education), School of Materials Science and Engineering, State Key Laboratory of Traction Power, Southwest Jiaotong University, Chengdu 610031, PR China

**Xiaodong Peng** – Key Laboratory of Advanced Technologies of Materials (Ministry of Education), School of Materials Science and Engineering, State Key Laboratory of Traction Power, Southwest Jiaotong University, Chengdu 610031, PR China

**Yue Gao** – Key Laboratory of Advanced Technologies of Materials (Ministry of Education), School of Materials Science and Engineering, State Key Laboratory of Traction Power, Southwest Jiaotong University, Chengdu 610031, PR China

**Qungui Wang** – Key Laboratory of Advanced Technologies of Materials (Ministry of Education), School of Materials Science and Engineering, State Key Laboratory of Traction Power, Southwest Jiaotong University, Chengdu 610031, PR China

**Jingjing Cao** – Key Laboratory of Advanced Technologies of Materials (Ministry of Education), School of Materials Science and Engineering, State Key Laboratory of Traction Power, Southwest Jiaotong University, Chengdu 610031, PR China

**Shiyu Yang** – Key Laboratory of Advanced Technologies of Materials (Ministry of Education), School of Materials Science and Engineering, State Key Laboratory of Traction Power, Southwest Jiaotong University, Chengdu 610031, PR China

Complete contact information is available at:

<https://pubs.acs.org/doi/10.1021/acs.jpcllett.2c00361>

### Notes

The authors declare no competing financial interest.

## ■ ACKNOWLEDGMENTS

This work is financially supported by the Young Scientific and Technological Innovation Research Team Funds of Sichuan Province (Nos. 20CXTD0106 and 2019YFG0292) and the Fundamental Research Funds for the Central Universities (No. 2682020CX06). The authors thank the Analysis and Testing Center of Southwest Jiaotong University for supporting the XRD, SEM, and DSC measurements. The authors gratefully acknowledge Ceshigo Research Service ([www.ceshigo.com](http://www.ceshigo.com)) for providing testing services.

## ■ REFERENCES

- (1) Xu, W.; Hu, Q.; Bai, S.; Bao, C.; Miao, Y.; Yuan, Z.; Borzda, T.; Barker, A. J.; Tyukalova, E.; Hu, Z.; Kawecki, M.; Wang, H.; Yan, Z.; Liu, X.; Shi, X.; Uvdal, K.; Fahlman, M.; Zhang, W.; Duchamp, M.; Liu, J.-M.; Petrozza, A.; Wang, J.; Liu, L.-M.; Huang, W.; Gao, F. Rational Molecular Passivation for High-Performance Perovskite Light-Emitting Diodes. *Nature Photonics*. **2019**, *13*, 418–424.
- (2) Gao, Y.; Yan, C.; Peng, X.; Li, W.; Cao, J.; Wang, Q.; Zeng, X.; Fu, X.; Yang, W. The Metal Doping Strategy in All Inorganic Lead Halide Perovskites: Synthesis, Physicochemical Properties, and Optoelectronic Applications. *Nanoscale*. **2021**, *13*, 18010–18031.
- (3) Cao, J.; Yan, C.; Luo, C.; Li, W.; Zeng, X.; Xu, Z.; Fu, X.; Wang, Q.; Chu, X.; Huang, H.; Zhao, X.; Lu, J.; Yang, W. Cryogenic-Temperature Thermodynamically Suppressed and Strongly Confined CsPbBr<sub>3</sub> Quantum Dots for Deeply Blue Light-Emitting Diodes. *Adv. Opt. Mater.* **2021**, *9*, 2100300.
- (4) Zeng, X.; Li, W.; Yan, C.; Cao, J.; Fu, X.; Yang, W. Crystallization Control via a Molecular Needle Knitting Strategy for the Enhanced Emission Efficiency and Stability of CsPbBr<sub>3</sub> Films. *J. Mater. Chem. C* **2021**, *9*, 15967–15976.
- (5) Peng, X.; Yan, C.; Chun, F.; Li, W.; Zeng, X.; Fu, X.; Gao, Y.; Chu, X.; Tian, G.; Yang, W. Liquid Nitrogen Passivation for Deep-Blue Perovskite Quantum Dots with Nearly Unit Quantum Yield. *J. Phys. Chem. C* **2022**, *126*, 1017–1025.
- (6) Gao, Y.; Luo, C.; Yan, C.; Li, W.; Liu, C.; Yang, W. Copper-Doping Defect-Lowered Perovskite Nanosheets for Deep-Blue Light-Emitting Diodes. *J. Colloid Interface Sci.* **2022**, *607*, 1796–1804.
- (7) Yang, W. Q.; Liu, H. G.; Liu, G. K.; Lin, Y.; Gao, M.; Zhao, X. Y.; Zheng, W. C.; Chen, Y.; Xu, J.; Li, L. Z. Trivalent Europium-Doped Strontium Molybdate Red Phosphors in White Light-Emitting Diodes: Synthesis, Photophysical Properties and Theoretical Calculations. *Acta Mater.* **2012**, *60*, 5399–5407.

- (8) Yang, W. Q.; Liu, H. G.; Gao, M.; Bai, Y.; Zhao, J.-T.; Xu, X.-D.; Wu, B.; Zheng, W.-C.; Liu, G.-K.; Lin, Y. Dual-Luminescence-Center Single-Component White-Light  $\text{Sr}_2\text{V}_2\text{O}_7\text{:Eu}^{3+}$  Phosphors for White Leds. *Acta Mater.* **2013**, *61*, 5096–5104.
- (9) Bi, C.; Yao, Z.; Sun, X.; Wei, X.; Wang, J.; Tian, J. Perovskite Quantum Dots with Ultralow Trap Density by Acid Etching-Driven Ligand Exchange for High Luminance and Stable Pure-Blue Light-Emitting Diodes. *Adv. Mater.* **2021**, *33*, 2006722.
- (10) Kim, Y. H.; Kim, S.; Kakekhani, A.; Park, J.; Park, J.; Lee, Y. H.; Xu, H.; Nagane, S.; Wexler, R. B.; Kim, D. H.; Jo, S. H.; Martínez Sarti, L.; Tan, P.; Sadhanala, A.; Park, G.-S.; Kim, Y. W.; Hu, B.; Bolink, H. J.; Yoo, S.; Friend, R. H.; Rappe, A. M.; Lee, T. W. Comprehensive Defect Suppression in Perovskite Nanocrystals for High-Efficiency Light-Emitting Diodes. *Nature Photonics*. **2021**, *15*, 148–155.
- (11) Luo, C.; Yan, C.; Li, W.; Chun, F.; Xie, M.; Zhu, Z.; Gao, Y.; Guo, B.; Yang, W. Ultrafast Thermodynamic Control for Stable and Efficient Mixed Halide Perovskite Nanocrystals. *Adv. Funct. Mater.* **2020**, *30*, 2000026.
- (12) Ke, W.; Spanopoulos, I.; Stoumpos, C. C.; Kanatzidis, M. G. Myths and Reality of  $\text{HPbI}_3$  in Halide Perovskite Solar Cells. *Nat. Commun.* **2018**, *9*, 4785.
- (13) Yao, Z.; Zhao, W.; Liu, S. Stability of the  $\text{CsPbI}_3$  Perovskite: from Fundamentals to Improvements. *J. Mater. Chem. A* **2021**, *9*, 11124–11144.
- (14) Masi, S.; Gualdrón-Reyes, A. F.; Mora-Seró, I. Stabilization of Black Perovskite Phase in  $\text{FAPbI}_3$  and  $\text{CsPbI}_3$ . *ACS Energy Lett.* **2020**, *5*, 1974–1985.
- (15) Xiang, S.; Fu, Z.; Li, W.; Wei, Y.; Liu, J.; Liu, H.; Zhu, L.; Zhang, R.; Chen, H. Highly Air-Stable Carbon-Based  $\alpha$ - $\text{CsPbI}_3$  Perovskite Solar Cells with a Broadened Optical Spectrum. *ACS Energy Lett.* **2018**, *3*, 1824–1831.
- (16) Chen, D.; Huang, D.; Yang, M.; Xu, K.; Hu, J.; Xu, F.; Liang, S.; Zhu, H. Room-Temperature Direct Synthesis of Tetragonal  $\beta$ - $\text{CsPbI}_3$  Nanocrystals. *Adv. Optical Mater.* **2022**, *10*, 2101869.
- (17) Antami, K.; Bateni, F.; Ramezani, M.; Hauke, C. E.; Castellano, F. N.; Abolhasani, M.  $\text{CsPbI}_3$  Nanocrystals Go with the Flow: From Formation Mechanism to Continuous Nanomanufacturing. *Adv. Funct. Mater.* **2022**, *32*, 2108687.
- (18) Zhang, J.; Yin, C.; Yang, F.; Yao, Y.; Yuan, F.; Chen, H.; Wang, R.; Bai, S.; Tu, G.; Hou, L. Highly Luminescent and Stable  $\text{CsPbI}_3$  Perovskite Nanocrystals with Sodium Dodecyl Sulfate Ligand Passivation for Red-Light-Emitting Diodes. *J. Phys. Chem. Lett.* **2021**, *12*, 2437–2443.
- (19) Chen, C.; Xuan, T.; Bai, W.; Zhou, T.; Huang, F.; Xie, A.; Wang, L.; Xie, R. J. Highly Stable  $\text{CsPbI}_3\text{:Sr}^{2+}$  Nanocrystals with Near-Unity Quantum Yield Enabling Perovskite Light-Emitting Diodes with an External Quantum Efficiency of 17.1%. *Nano Energy*. **2021**, *85*, 106033.
- (20) Lu, M.; Guo, J.; Sun, S.; Lu, P.; Wu, J.; Wang, Y.; Kershaw, S. V.; Yu, W. W.; Rogach, A. L.; Zhang, Y. Bright  $\text{CsPbI}_3$  Perovskite Quantum Dot Light-Emitting Diodes with Top-Emitting Structure and a Low Efficiency Roll-Off Realized by Applying Zirconium Acetylacetonate Surface Modification. *Nano Lett.* **2020**, *20*, 2829–2836.
- (21) Lan, Y. F.; Yao, J. S.; Yang, J. N.; Song, Y. H.; Ru, X. C.; Zhang, Q.; Feng, L. Z.; Chen, T.; Song, K. H.; Yao, H. B. Spectrally Stable and Efficient Pure Red  $\text{CsPbI}_3$  Quantum Dot Light-Emitting Diodes Enabled by Sequential Ligand Post-Treatment Strategy. *Nano Lett.* **2021**, *21*, 8756–8763.
- (22) Shen, X.; Zhang, Y.; Kershaw, S. V.; Li, T.; Wang, C.; Zhang, X.; Wang, W.; Li, D.; Wang, Y.; Lu, M.; Zhang, L.; Sun, C.; Zhao, D.; Qin, G.; Bai, X.; Yu, W. W.; Rogach, A. L. Zn-Alloyed  $\text{CsPbI}_3$  Nanocrystals for Highly Efficient Perovskite Light-Emitting Devices. *Nano Lett.* **2019**, *19*, 1552–1559.
- (23) Li, H.; Lin, H.; Ouyang, D.; Yao, C.; Li, C.; Sun, J.; Song, Y.; Wang, Y.; Yan, Y.; Wang, Y.; Dong, Q.; Choy, W. C. H. Efficient and Stable Red Perovskite Light-Emitting Diodes with Operational Stability > 300 h. *Adv. Mater.* **2021**, *33*, 2008820.
- (24) Cheng, G.; Liu, Y.; Chen, T.; Chen, W.; Fang, Z.; Zhang, J.; Ding, L.; Li, X.; Shi, T.; Xiao, S. Efficient All-Inorganic Perovskite Light-Emitting Diodes with Improved Operation Stability. *ACS Appl. Mater. Interfaces* **2020**, *12*, 18084–18090.
- (25) Chen, Z.; Zhou, B.; Yuan, J.; Tang, N.; Lian, L.; Qin, L.; Zhu, L.; Zhang, J.; Chen, R.; Zang, J.  $\text{Cu}^{2+}$ -Doped  $\text{CsPbI}_3$  Nanocrystals with Enhanced Stability for Light-Emitting Diodes. *J. Phys. Chem. Lett.* **2021**, *12*, 3038–3045.
- (26) Pan, J.; Shang, Y.; Yin, J.; De Bastiani, M.; Peng, W.; Dursun, I.; Sinatra, L.; El-Zohry, A. M.; Hedhili, M. N.; Emwas, A. H.; Mohammed, O. F.; Ning, Z.; Bakr, O. M. Bidentate Ligand-Passivated  $\text{CsPbI}_3$  Perovskite Nanocrystals for Stable Near-Unity Photoluminescence Quantum Yield and Efficient Red Light-Emitting Diodes. *J. Am. Chem. Soc.* **2018**, *140*, 562–565.
- (27) Pan, G.; Bai, X.; Shen, X.; Wang, L.; Mao, Y.; Chen, X.; Xu, W.; Shao, H.; Zhou, D.; Dong, B.; Xu, L.; Hu, J.; Song, H. Bright Red  $\text{YCl}_3$ -Promoted  $\text{CsPbI}_3$  Perovskite Nanorods towards Efficient Light-Emitting Diode. *Nano Energy*. **2021**, *81*, 105615.
- (28) Hassan, Y.; Park, J. H.; Crawford, M. L.; Sadhanala, A.; Lee, J.; Sadighian, J. C.; Mosconi, E.; Shivanna, R.; Radicchi, E.; Jeong, M.; Yang, C.; Choi, H.; Park, S. H.; Song, M. H.; De Angelis, F.; Wong, C. Y.; Friend, R. H.; Lee, B. R.; Snaith, H. J. Ligand-Engineered Bandgap Stability in Mixed-Halide Perovskite Leds. *Nature*. **2021**, *591*, 72–77.
- (29) Kuang, C.; Hu, Z.; Yuan, Z.; Wen, K.; Qing, J.; Kobera, L.; Abbrent, S.; Brus, J.; Yin, C.; Wang, H.; Xu, W.; Wang, J.; Bai, S.; Gao, F. Critical Role of Additive-Induced Molecular Interaction on the Operational Stability of Perovskite Light-Emitting Diodes. *Joule*. **2021**, *5*, 618–630.
- (30) Ji, Y.; Zhang, J. B.; Shen, H. R.; Su, Z.; Cui, H.; Lan, T.; Wang, J. Q.; Chen, Y. H.; Liu, L.; Cao, K.; Shen, W.; Chen, S. Improving the Stability of  $\alpha$ - $\text{CsPbI}_3$  Nanocrystals in Extreme Conditions Facilitated by  $\text{Mn}^{2+}$  Doping. *ACS Omega*. **2021**, *6*, 13831–13838.
- (31) Cho, H.; Kim, Y. H.; Wolf, C.; Lee, H. D.; Lee, T. W. Improving the Stability of Metal Halide Perovskite Materials and Light-Emitting Diodes. *Adv. Mater.* **2018**, *30*, 1704587.
- (32) Fang, Z.; Chen, W.; Shi, Y.; Zhao, J.; Chu, S.; Zhang, J.; Xiao, Z. Dual Passivation of Perovskite Defects for Light-Emitting Diodes with External Quantum Efficiency Exceeding 20%. *Adv. Funct. Mater.* **2020**, *30*, 1909754.
- (33) Ke, Y.; Wang, N.; Kong, D.; Cao, Y.; He, Y.; Zhu, L.; Wang, Y.; Xue, C.; Peng, Q.; Gao, F.; Huang, W.; Wang, J. Defect Passivation for Red Perovskite Light-Emitting Diodes with Improved Brightness and Stability. *J. Phys. Chem. Lett.* **2019**, *10*, 380–385.
- (34) Lu, R.; Liu, Y.; Zhang, J.; Zhao, D.; Guo, X.; Li, C. Highly Efficient (200) Oriented  $\text{MAPbI}_3$  Perovskite Solar Cells. *Chem. Eng. J.* **2022**, *433*, 133845.
- (35) Ding, X.; Chen, H.; Wu, Y.; Ma, S.; Dai, S.; Yang, S.; Zhu, J. Triple Cation Additive  $\text{NH}_4^+\text{C}_2\text{H}_4\text{NH}_3^+\text{C}_2\text{H}_4\text{NH}_3^+$ -Induced Phase-Stable Inorganic  $\alpha$ - $\text{CsPbI}_3$  Perovskite Films for use in Solar Cells. *J. Mater. Chem. A* **2018**, *6*, 18258–18266.
- (36) Xue, D. J.; Hou, Y.; Liu, S. C.; Wei, M.; Chen, B.; Huang, Z.; Li, Z.; Sun, B.; Proppe, A. H.; Dong, Y.; Saidaminov, M. I.; Kelley, S. O.; Hu, J. S.; Sargent, E. H. Regulating Strain in Perovskite Thin Films through Charge-Transport Layers. *Nat. Commun.* **2020**, *11*, 1514.
- (37) Sun, G.; Liu, X.; Liu, Z.; Liu, D.; Meng, F.; Li, Z.; Chu, L.; Qiu, W.; Peng, X.; Xie, W.; Shen, C.; Chen, J.; Yip, H. L.; Su, S. J. Emission Wavelength Tuning via Competing Lattice Expansion and Octahedral Tilting for Efficient Red Perovskite Light-Emitting Diodes. *Adv. Funct. Mater.* **2021**, *31*, 2106691.
- (38) Wang, H.; Zhu, C.; Liu, L.; Ma, S.; Liu, P.; Wu, J.; Shi, C.; Du, Q.; Hao, Y.; Xiang, S.; Chen, H.; Chen, P.; Bai, Y.; Zhou, H.; Li, Y.; Chen, Q. Interfacial Residual Stress Relaxation in Perovskite Solar Cells with Improved Stability. *Adv. Mater.* **2019**, *31*, 1904408.
- (39) Sutton, R. J.; Filip, M. R.; Haghghirad, A. A.; Sakai, N.; Wenger, B.; Giustino, F.; Snaith, H. J. Cubic or Orthorhombic? Revealing the Crystal Structure of Metastable Black-Phase  $\text{CsPbI}_3$  by Theory and Experiment. *ACS Energy Lett.* **2018**, *3*, 1787–1794.
- (40) Zhang, Y.; Siegler, T. D.; Thomas, C. J.; Abney, M. K.; Shah, T.; De Gorostiza, A.; Greene, R. M.; Korgel, B. A. A “Tips and Tricks”



Practical Guide to the Synthesis of Metal Halide Perovskite Nanocrystals. *Chem. Mater.* **2020**, *32*, 5410–5423.

(41) Dang, Z.; Shamsi, J.; Palazon, F.; Imran, M.; Akkerman, Q. A.; Park, S.; Bertoni, G.; Prato, M.; Brescia, R.; Manna, L. In Situ Transmission Electron Microscopy Study of Electron Beam-Induced Transformations in Colloidal Cesium Lead Halide Perovskite Nanocrystals. *ACS Nano* **2017**, *11*, 2124–2132.

(42) Li, F.; Liu, Y.; Wang, H. L.; Zhan, Q.; Liu, Q. L.; Xia, Z. G. Postsynthetic Surface Trap Removal of CsPbX<sub>3</sub> (X = Cl, Br, or I) Quantum Dots via a ZnX<sub>2</sub>/Hexane Solution toward an Enhanced Luminescence Quantum Yield. *Chem. Mater.* **2018**, *30*, 8546–8554.

(43) Pei, Y.; Liu, Y.; Li, F.; Bai, S.; Jian, X.; Liu, M. Unveiling Property of Hydrolysis-Driven DMAPbI<sub>3</sub> for Perovskite Devices: Composition Engineering, Defect Mitigation, and Stability Optimization. *iScience* **2019**, *15*, 165–172.

(44) Bian, H.; Wang, H.; Li, Z.; Zhou, F.; Xu, Y.; Zhang, H.; Wang, Q.; Ding, L.; Liu, S. F.; Jin, Z. Unveiling the Effects of Hydrolysis-Derived DMAI/DMAPIx Intermediate Compound on the Performance of CsPbI<sub>3</sub> Solar Cells. *Adv. Sci. (Weinh)* **2020**, *7*, 1902868.

(45) Wu, Y.; Wei, C.; Li, X.; Li, Y.; Qiu, S.; Shen, W.; Cai, B.; Sun, Z.; Yang, D.; Deng, Z.; Zeng, H. In Situ Passivation of PbBr<sub>6</sub><sup>4-</sup> Octahedra toward Blue Luminescent CsPbBr<sub>3</sub> Nanoplatelets with Near 100% Absolute Quantum Yield. *ACS Energy Lett.* **2018**, *3*, 2030–2037.

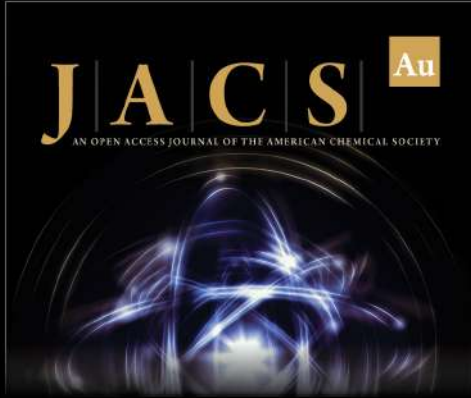
(46) Cai, Y.; Wang, H.; Li, Y.; Wang, L.; Lv, Y.; Yang, X.; Xie, R. J. Trimethylsilyl Iodine-Mediated Synthesis of Highly Bright Red-Emitting CsPbI<sub>3</sub> Perovskite Quantum Dots with Significantly Improved Stability. *Chem. Mater.* **2019**, *31*, 881–889.

(47) Saran, R.; Heuer-Jungemann, A.; Kanaras, A. G.; Curry, R. J. Giant Bandgap Renormalization and Exciton–Phonon Scattering in Perovskite Nanocrystals. *Adv. Opt. Mater.* **2017**, *5*, 1700231.

(48) Wright, A. D.; Verdi, C.; Milot, R. L.; Eperon, G. E.; Perez-Osorio, M. A.; Snaith, H. J.; Giustino, F.; Johnston, M. B.; Herz, L. M. Electron-Phonon Coupling in Hybrid Lead Halide Perovskites. *Nat. Commun.* **2016**, *7*, 11755.


(49) Burwig, T.; Fränzel, W.; Pistor, P. Crystal Phases and Thermal Stability of Co-evaporated CsPbX<sub>3</sub> (X = I, Br) Thin Films. *J. Phys. Chem. Lett.* **2018**, *9*, 4808–4813.


(50) Chiba, T.; Hayashi, Y.; Ebe, H.; Hoshi, K.; Sato, J.; Sato, S.; Pu, Y.-J.; Ohisa, S.; Kido, J. Anion-Exchange Red Perovskite Quantum Dots with Ammonium Iodine Salts for Highly Efficient Light-Emitting Devices. *Nature Photonics* **2018**, *12*, 681–687.



**JACS** Au  
AN OPEN ACCESS JOURNAL OF THE AMERICAN CHEMICAL SOCIETY

Editor-in-Chief  
**Prof. Christopher W. Jones**  
Georgia Institute of Technology, USA

**Open for Submissions** 

pubs.acs.org/jacsau  ACS Publications  
Most Trusted. Most Cited. Most Read.